



Technical Note

# The Temporal Variation of Optical Depth in the Candidate Landing Area of China's Mars Mission (Tianwen-1)

Zhencheng Tang <sup>1,2</sup> , Jianjun Liu <sup>1,2,\*</sup>, Xing Wang <sup>1,2</sup>, Xin Ren <sup>1</sup>, Wei Yan <sup>1</sup> and Wangli Chen <sup>1</sup>

- <sup>1</sup> Key Laboratory of Lunar and Deep Space Exploration, National Astronomical Observatories, Chinese Academy of Sciences, Beijing 100101, China; tangzhencheng@nao.cas.cn (Z.T.); wangx01@nao.cas.cn (X.W.); renx@nao.cas.cn (X.R.); yanw@nao.cas.cn (W.Y.); chenwl@nao.cas.cn (W.C.)
- <sup>2</sup> School of Astronomy and Space Science, University of Chinese Academy of Sciences, Beijing 100049, China
- \* Correspondence: liujj@nao.cas.cn

**Abstract:** The atmospheric dust is an important factor in the evolution of the Martian climate and has a major impact on the scientific exploration of the Martian lander or rover and its payload. This paper used remote sensing images to calculate atmospheric optical depth that characterizes the spatial distribution of the atmospheric dust of Mars. The optical depth calculated by the images of the High Resolution Imaging Science Experiment (HiRISE) in the inspection area of the Spirit rover had a similar temporal variation to the optical depth directly measured by the Spirit rover from the sunlight decay. We also used the HiRISE images to acquire the seasonal variation of optical depths in the candidate landing area of China's Mars Mission (Tianwen-1). The results have shown that the seasonal pattern of the optical depth in the candidate landing area is consistent with the dust storm sequences in this area. After Tianwen-1 enters the orbit around Mars, the images collected by the Moderate Resolution Imaging Camera (MoRiC), and the High Resolution Imaging Camera (HiRIC) can be used to study the atmospheric optical depth in the candidate landing area, providing reference for the safe landing and operation of the lander and rover.

**Keywords:** remote sensing images; temporal variation of optical depth; Tianwen-1; candidate landing area



**Citation:** Tang, Z.; Liu, J.; Wang, X.; Ren, X.; Yan, W.; Chen, W. The Temporal Variation of Optical Depth in the Candidate Landing Area of China's Mars Mission (Tianwen-1). *Remote Sens.* **2021**, *13*, 1029. <https://doi.org/10.3390/rs13051029>

Academic Editor: Giancarlo Bellucci

Received: 27 January 2021  
Accepted: 5 March 2021  
Published: 9 March 2021

**Publisher's Note:** MDPI stays neutral with regard to jurisdictional claims in published maps and institutional affiliations.



**Copyright:** © 2021 by the authors. Licensee MDPI, Basel, Switzerland. This article is an open access article distributed under the terms and conditions of the Creative Commons Attribution (CC BY) license (<https://creativecommons.org/licenses/by/4.0/>).

## 1. Introduction

The Martian wind is only the last element in a chain of causation that generates storms (especially global dust storms) and alters the spatial distribution of the atmospheric dust [1]. The Martian atmospheric dust actively participates in the evolution process of Martian climate and also provides a long-term effect on the morphology and albedo of the Martian surface due to the dust denudation, migration, and deposition [2]. In addition, the spatial distribution of atmospheric dust has an obvious impact on the remote sensing images acquired by orbiters, landers, and rovers in Mars missions, such as reducing the information content of an image and the ability to discern surface characteristics [3]. Moreover, the atmospheric dust environment on Mars has a significant influence on the Mars lander and rover and their payloads. When the dust deposited on the surface of the solar cell array and optical sensors of the probe landing on the Martian surface will directly affect the efficiency and service life expectancy of the energy systems and the optical properties and image quality of optical sensors [4]. Therefore, studying the spatial and temporal variation mechanism of the Martian atmospheric dust could help us better understand the Martian climatic environment, provide guidance for Mars missions in the future, and data assimilation of airborne dust is carried out to improve the numerical simulation of the Martian climate model [5,6].

The optical depth of the Martian atmosphere is mainly determined by aerosols. Most Martian aerosols are dust particles that present reddish in images [7,8]. The spatial and temporal distribution of atmospheric dust can thus be represented by the variation of

atmospheric optical depth. The variation of the optical depth in images taken from different times can reflect the variation of the spatial distribution of atmospheric dust. Therefore, it is necessary to understand the spatial distribution and variation of atmospheric dust in the specific area for the landing and inspection of the Mars probe. The research of the variation of optical depth can provide a reference for these engineering applications and also has important application value for the operation and service life expectancy of the lander and the rover.

Two approaches for calculating the atmospheric optical depth in the Mars missions based on different data sources are in active use. One is on the remote sensing data of the orbiter. Smith [9] retrieved dust optical depth based on limb-geometry observations from Thermal Emission Spectrometer (TES) and found that a higher degree of interannual variability of dust optical depth during the perihelion season than that during the aphelion season. Vincendon et al. [10] used the Monte Carlo method to calculate the surface albedo based on OMEGA/Mars Express dataset of low to mid-latitude regions on the Martian surface, and then used the look-up table to retrieve optical depth. They compared the results with the measurement of optical depth obtained by the Mars Exploration Rovers (MER) and demonstrated that the apparent albedo variations on the Martian surface were consistent with the variations of the optical depth of atmospheric dust in the corresponding area, and the construction of the look-up table involved radiation parameters, observation geometry, surface reflectance, and detailed atmospheric aerosol model. However, the band and resolution of images are mainly concerned in the retrieval procedure of the optical depth in this paper. Smith [11] used the surface temperature information obtained from the Thermal Emission Imaging System (THEMIS) data. Then, based on the relationship between the temperature and optical depth, he used the linear fitting method to estimate the optical depth and compared it with the optical depth obtained by Mars Global Surveyor (MGS), Mars Express, and MRO dataset, and Smith [12] showed the spatial and temporal variation of dust optical depth before and after the global dust storm based on observations taken by THEMIS. In addition, based on the images of High Resolution Stereo Cameras (HRSC) and High Resolution Imaging Science Experiment (HiRISE), Hoekzema et al. [13] calculated the optical depth by using the radiance difference between the shadowed and the adjacent sunlit regions of the image and established the correlation between the elevation and the optical depth. Montabone et al. [14] obtained the gridded maps of dust optical depth using the method of iterative weighted binning based on observations from TES, THEMIS, and Mars Climate Sounder (MCS) and presented the interannual and seasonal variability of dust optical depth over eight Martian years.

The other one to calculate the optical depth was to use the data acquired by the rovers. During the MER mission, the rover's panoramic cameras captured pictures of the Sun to directly measure the solar radiation and the optical depth was derived from these data [15,16]. The same approach was also employed calculate the optical depth from the in situ data of Viking Lander and Pathfinder [17,18]. Previous studies have shown that the optical depth calculated from the remote sensing images of the orbiter is smaller than that obtained by the rover's data (the correction coefficient between these two optical depths measurements is about 0.7), which is probably largely because the diffuse radiation received by the shadow and sunlit areas assumed in the theory may not be equal actually [13].

In this paper, the retrieval procedure of the optical depth is established to prepare for the analysis of the optical depth in the candidate landing area of Tianwen-1 using MoRIC and HiRIC images. The optical depth of the inspection area of the Spirit rover is calculated using the shadow method based on HiRISE images [13]. The results are compared with the optical depth measured by the Spirit rover [15,16]. Then, the optical depth in the candidate landing area of Tianwen-1 is also retrieved by using the shadow method based on the HiRISE images. In Section 2, the dataset and the method of retrieving optical depth are introduced, including the calculation method by using the remote sensing image of the orbiter. Additionally, we also introduce the data of optical depth calculated by using the direct measurement of solar decay by the Spirit rover. The results are presented in

Section 3, including the comparison between the optical depth obtained by the remote sensing image and the optical depth retrieved from the data of the Spirit rover in the same Martian year. Then the temporal variation of optical depth in the candidate landing area of Tianwen-1 is obtained by HiRISE images. In Section 4, we summarize the findings and make some prospects.

## 2. Data and Methods

### 2.1. Description of Dataset

HiRISE onboard MRO has been imaging the Martian surface since November 2006. The spatial resolution of HiRISE images is 0.25–0.5 m/pixel [19]. The central band of the red image obtained through the red filter is 700 nm (the band range is 550–850 nm), and the width of the image is about 6 km (the orbital altitude is 300 km). The width of color images obtained from blue-green (400–600 nm), red, and near-infrared (800–1000 nm) is about 1.2 km. In this paper, the imagery data products after preprocessing are selected. The preprocessing process includes radiometric calibration and geometric correction. The DN (Digital Number) of the image is converted to radiance after dark current correction, instrument offset, and gain correction. The optical distortion is corrected by geometric processing, and the image acquired by the orbiter was projected onto the map coordinate system. The images obtained by the orbiter from the Martian surface between 65°S and 65°N were employed by the Equirectangular map projection, while the Polar Stereographic projection was used for the images above 65 degrees to the poles [20]. The incidence angle and the emission angle of the image can be retrieved from the Planetary Data System (PDS), and the HiRISE image can be downloaded at <https://hirise-pds.lpl.arizona.edu/PDS/> (accessed on 15 January 2021). The HiRISE images selected in this paper are shown in Table 1.

**Table 1.** List of related High Resolution Imaging Science Experiment (HiRISE) images.

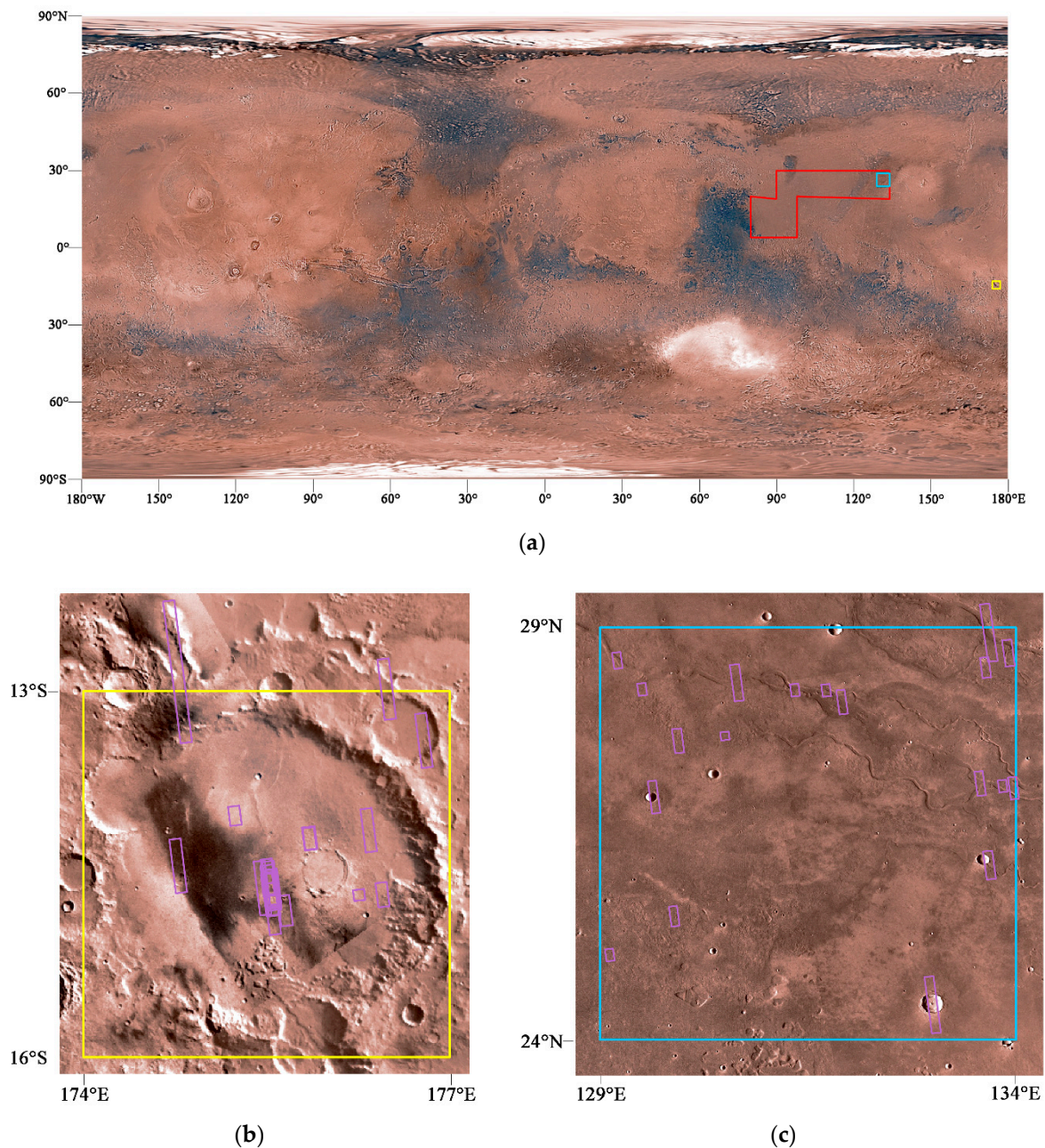
Study Area	Product ID	Observation Time	Martian Year (MY)	Solar Longitude (Ls)
The inspection area of the Spirit rover	PSP_006524_1650_RED	2007-12-17	29	4.0
	PSP_006735_1650_RED	2008-01-03	29	12.0
	PSP_007737_1670_RED	2008-03-21	29	48.0
	PSP_007816_1665_RED	2008-03-27	29	50.7
	PSP_008317_1665_RED	2008-05-05	29	67.8
	PSP_008528_1660_RED	2008-05-21	29	75.0
	PSP_008963_1650_RED	2008-06-24	29	89.9
	PSP_009174_1650_RED	2008-07-11	29	97.1
	PSP_009319_1650_RED	2008-07-22	29	102.2
	PSP_009385_1655_RED	2008-07-27	29	104.5
	PSP_009741_1655_RED	2008-08-24	29	117.2
	PSP_009886_1655_RED	2008-09-04	29	122.5
	PSP_010097_1655_RED	2008-09-21	29	130.3
	ESP_011587_1655_RED	2009-01-15	29	191.8
	ESP_011943_1650_RED	2009-02-12	29	208.3
	ESP_012787_1650_RED	2009-04-18	29	249.4
	ESP_012932_1650_RED	2009-04-30	29	256.6
	ESP_013499_1650_RED	2009-06-13	29	284.3
	ESP_013855_1650_RED	2009-07-11	29	301.2
	ESP_013921_1650_RED	2009-07-16	29	304.2
ESP_014277_1650_RED	2009-08-12	29	320.3	

Table 1. Cont.

Study Area	Product ID	Observation Time	Martian Year (MY)	Solar Longitude (Ls)
The study area (part of the candidate landing area of Tianwen-1)	PSP_005721_2090_RED	2007-10-16	28	331.5
	PSP_006776_2070_RED	2008-01-06	29	13.6
	PSP_007422_2085_RED	2008-02-25	29	37.0
	PSP_007501_2065_RED	2008-03-02	29	39.7
	PSP_007791_2090_RED	2008-03-25	29	49.8
	PSP_008503_2045_RED	2008-05-20	29	74.1
	ESP_017852_2080_RED	2010-05-18	30	92.4
	ESP_024656_2085_RED	2011-10-30	31	22.7
	ESP_027557_2075_RED	2012-06-12	31	123.9
	ESP_045359_2075_RED	2016-03-30	33	130.2
	ESP_048049_2060_RED	2016-10-26	33	249.2
	ESP_054800_2075_RED	2018-04-05	34	154.5
	ESP_054866_2085_RED	2018-04-10	34	157.2
	ESP_057649_2055_RED	2018-11-13	34	287.5
	ESP_057728_2090_RED	2018-11-19	34	291.3
	ESP_058137_2090_RED	2018-12-21	34	310.3
	ESP_064163_2085_RED	2020-04-04	35	177.5
	ESP_064229_2085_RED	2020-04-09	35	180.4
	ESP_066049_2080_RED	2020-08-29	35	267.3

The Spirit rover landed in the Gusev crater (14.57°S, 175.48°E) on 4 January 2004, and began its exploration mission, which ended on 22 March 2010 [21]. The Panorama Camera of the Spirit rover is equipped with two special solar filters designed to study atmospheric optical depth. The Spirit rover used these two special solar filters to photograph the Sun directly several times per day, which could measure the decay of sunlight to obtain the optical depth of the Martian atmosphere. The central band of the red filter is 880 nm, and the central band of the blue filter is 440 nm. However, due to a red leakage, the actual central response band of the blue filter is consistent with the band of 719 nm, so the blue filter was considered to be centered at 719 nm [15]. The optical depth of the rover is obtained by analyzing the panorama camera images. Space-borne radiometric calibration and geometric calibration were carried out, and afterwards relative radiometric calibration was carried out using observation data with a similar observation time. The uncertainties generated by radiometric calibration of measured data were compared and verified with the uncertainties generated by laboratory calibration. The results showed that these two uncertainties were consistent [22]. Therefore, when a large amount of measured data is obtained, the data processing of retrieving optical depth based on these data is consistent with the data processing in previous laboratory tests [15]. The data products of the optical depth are available on [https://pds-geosciences.wustl.edu/mer/mer1\\_mer2-m-pancam-5-atmos-opacity-v1/merao\\_1xxx/data/](https://pds-geosciences.wustl.edu/mer/mer1_mer2-m-pancam-5-atmos-opacity-v1/merao_1xxx/data/) (accessed on 20 January 2021).

In order to facilitate comparison and verification, the data of optical depth measured in the 719 nm band by the Spirit rover in MY29 was selected. Meanwhile, the HiRISE red images in the inspection area (174°–177°E, 13°–16°S, as shown in the yellow rectangle in Figure 1) of Spirit rover in MY29 was collected, and the temporal variation of optical depth was calculated by using the shadow method based on these images. The time conversion table established by Clancy et al. [23] can be used to convert the Earth time of the corresponding data to the Martian time. In addition, the HiRISE red images of in the candidate landing area of China's Mars Mission (Tianwen-1) (the study area is 24°–29°N, 129°–134°E, as shown in the blue box in Figure 1) were collected, and the optical depth of this area was calculated by using the shadow method based on these remote sensing images, to obtain the temporal variation of the optical depth in this area.



**Figure 1.** The schematic diagram of the research area and the footprints of images. (a) The red polygon represents the candidate landing area of China’s Mars Mission (Tianwen-1) [24], the blue rectangle represents the study area (part of the candidate landing area), and the yellow rectangle represents the inspection area of the Spirit rover. The base map is global color mosaic of the Mars by Viking Orbiter [25]; (b) The footprints (purple rectangle) of images in the inspection area of the Spirit rover; (c) The footprints (purple rectangle) of images in the candidate landing area.

## 2.2. Methods

As the sunlight propagates through the atmospheric medium, it is weakened by the interaction (like scattering and absorption) with the atmospheric medium (such as dust). Optical depth is a dimensionless quantity that characterizes the radiation extinction by the atmospheric medium. The radiation brightness of a specific shadowed region in a remote sensing image contains the information of the atmospheric optical depth of the region. If optical depth in this region increases, the difference in radiation brightness between the shadowed and the adjacent sunlit regions will decrease. The radiation brightness difference

between the shadowed and the adjacent sunlit areas can be converted into the optical depth value using the shadow method, and the optical depth  $\tau_s$  is calculated by Equation (1) [13].

$$\tau_s = -\frac{\mu_0\mu}{\mu_0 + \mu} \ln\left(\frac{I_{sunlit} - I_{shadow}}{I_{sunlit}}\right) \quad (1)$$

Here,  $\mu_0$  is the cosine of the solar incidence angle and  $\mu$  is the cosine of the solar emission angle.  $I_{sunlit}$  is the intensity of radiation of the sunlit area and  $I_{shadow}$  is the intensity of radiation of the shadowed area. The radiance of the image is equal to the sum of the DN value of the image multiplied by the gain coefficient obtained by radiometric calibration and the offset coefficient obtained by radiometric calibration. The calculation of the optical depth using the shadow method is based on the following assumptions: Lambert reflection (ideal scattering) is performed on the surface of the shadowed and the sunlit areas. The atmospheric scattering characteristics on the shadowed and the sunlit areas are the same. The selected shadowed and the sunlit areas receive the same diffuse radiation. The surface albedo is similar to the albedo of the top of atmosphere. The shadowed and the sunlit areas have the same optical depth.

In the remote sensing images, the shadowed area (such as the backside of the slope and the backside of the cliff along the impact crater) and the adjacent sunlit area were selected, and the sunlit area with flat terrain was selected as far as possible through visual interpretation. Sampling lines were drawn in the shadowed and the sunlit areas, respectively (see Figure 2). In each case, the average radiance of the sampling lines in the corresponding area was extracted. Then, the optical depth  $\tau_s$  is calculated out by using Equation (1). The optical depth is related to the true optical depth measured by the rover and a correction coefficient could be applied to reckon the actual optical depth [13].

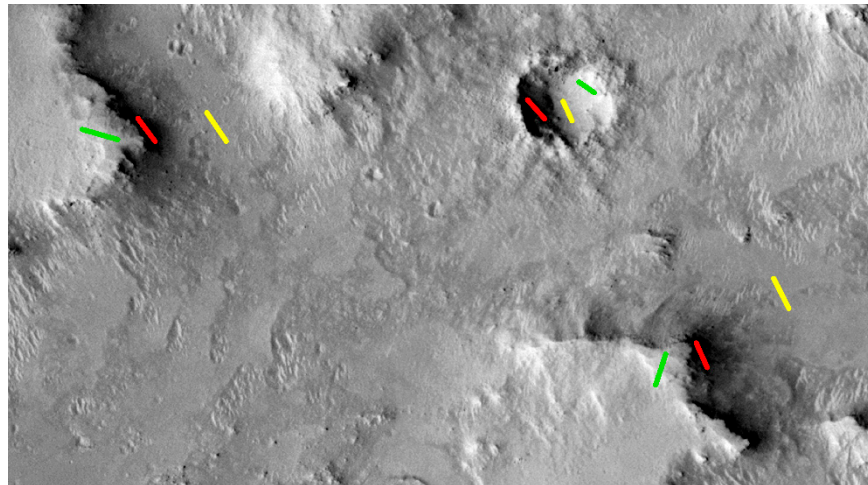


**Figure 2.** The schematic diagram of the selection of the shadowed and the adjacent sunlit areas (The image is part of the HiRISE image ESP\_013855\_1650. The red line indicates shadowed areas, the yellow line indicates flat sunlit areas, and the green line indicates the sunlit areas with obvious slope).

### 3. Results and Discussion

The Panoramic Camera onboard the Spirit rover takes pictures of the Sun directly to obtain the images with radiation flux. The optical depth was calculated by measuring the decay of sunlight based on the data of the panoramic cameras image, which can be used as the “ground truth value” of the optical depth in the inspection area of the Spirit rover. HiRISE red image is used to calculate the optical depth at different periods of the inspection area of the Spirit rover using the shadow method. Multiple pairs of shadowed areas and sunlit areas in each image were selected to calculate the optical depth, and the

mean value and standard deviation of the optical depth were calculated, which were used to draw the graph of the error bar.

In the process of calculating the optical depth based on the shadow method, the distance between the selected shadowed and the sunlit areas is less than several kilometers and the elevation difference between these two areas is less than hundreds of meters [13]. The shadowed and the adjacent sunlit areas have the similar atmospheric model and the law of surface reflection. The atmospheric scattering characteristics of the sunlit area and the shadowed area are also similar, and the sunlit and the shadowed areas receive the same diffuse radiation. Therefore, the error of optical depth mainly comes from the difference of diffuse radiation between the shadowed and the sunlit areas. For example, for the same shadowed area near the wall of an impact crater, the sunlit area near the wall of the impact crater and the sunlit area in the central region of the impact crater were each selected to calculate the optical depth. Due to the difference of slope between the area near the wall of the impact crater and the central area of the crater, the optical scattering characteristics of the corresponding sunlit area on the surface are different. Therefore, when the radiance difference between the shadowed and the sunlit areas is used to calculate the optical depth, the scattering characteristics are inconsistent due to the difference of the apparent geometry conditions (such as the slope), which leads to the error in the calculation of the optical depth. Multiple pairs of shadowed areas and sunlit areas in each image were selected (see Figure 2). For the same shadowed area, the sunlit area with obvious slope and the sunlit area with relatively flat terrain were selected to calculate the optical depth, respectively, and the relative error of these two optical depth values was calculated (take the flat sunlit area as a reference). All these relative errors were counted and the range of these relative errors was obtained.

For comparative verification and analysis, the optical depth of the inspection area of the Spirit rover calculated by the shadow method based on remote sensing images was compared with the optical depth measured by the data of the Spirit rover in the same Martian year (MY29). The corresponding relationship between optical depth and solar longitude (Ls) in the same Martian year is established (see Figure 3). According to statistical analysis, for the same shadowed area, the relative error of the retrieved optical depth is between 8% and 13% by selecting the sunlit area with obvious slope and the sunlit area with relatively flat terrain. As can be seen in Figure 3, in the same Martian year, the optical depth calculated by using the remote sensing image of the orbiter in the inspection area of Spirit rover has a similar temporal variation with the optical depth obtained by the data of Spirit rover. The optical depth in the period during Ls~150 to 330° is larger than that in the period during Ls~30 to 130°. Studies have found that dust storm activities are more frequent in the southern hemisphere of Mars during Ls~135 to 305° [1]. The dust generally experiences repeatable seasonal variations generally and the perihelion season (roughly Ls~180 to 360°) is relatively dustier than the aphelion season (roughly Ls~0 to 180°) [9,26]. The height above surface of vertical distribution of dust in the perihelion season is higher than that in the aphelion season [27], and the number of dust storm activity recorded in the Mars Dust Activity Database have shown that most of dust activity occur in fall and winter in the southern hemisphere [28]. It can be seen that a great amount of dust storm activity lead to an increase in the amount of dust in the atmosphere, which causes the increase of optical depth, so that the optical depth in the period of larger amount of dust activity (Ls~150 to 330°) is higher than that in the period of smaller amount of dust activity (Ls~30 to 130°). In addition, the optical depth calculated by the shadow method in this paper is smaller than that obtained by the data of the rover, and the correction coefficient between these two measurements of optical depth is  $0.638 \pm 0.071$  (i.e.,  $\tau_s / \tau_{Spirit} = 0.638 \pm 0.071$ ), which shows that the correction coefficient obtained in this paper is similar to that obtained in the previous studies [13]. The correction result of the optical depth divided by the correction coefficient is shown in Figure 3, which shows that the corrected optical depth is consistent with the “ground truth value”.

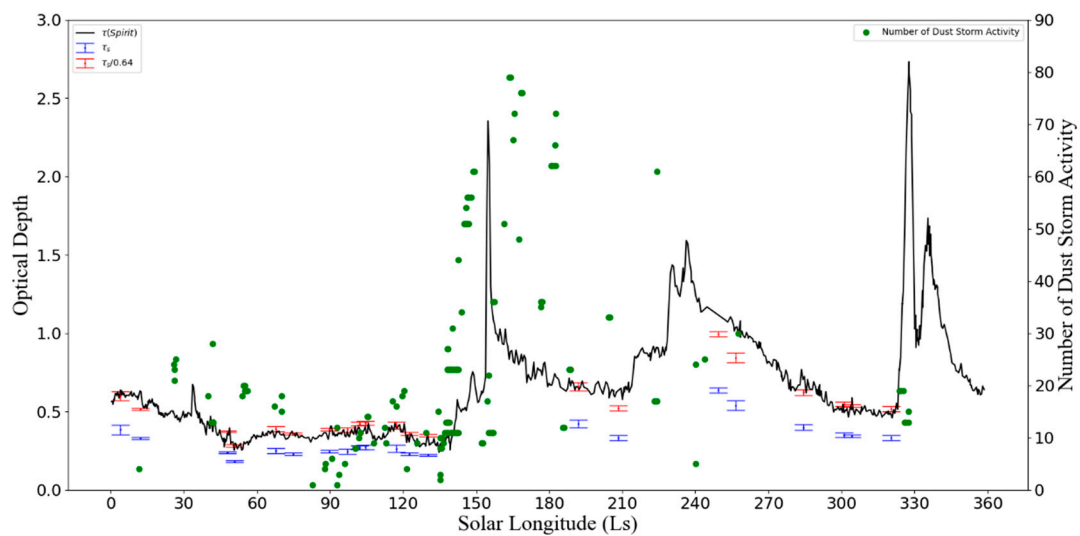


**Figure 3.** The distribution of optical depth at different solar longitudes in MY29 (the blue error bars represents the optical depth of the inspection area of the Spirit rover calculated by the shadow method, the red error bars represents the optical depth divided by the correction coefficient, the black line represents the optical depth measured by the data of the Spirit rover [16], and green dots represents the number of dust storm activity recorded in the Mars Dust Activity Database (MDAD) at  $0^{\circ}$ – $30^{\circ}$ S in MY29 [28]).

The optical depth is calculated by the shadow method based on HiRISE red images in the candidate landing area of China's Mars Mission (Tianwen-1). Further, multiple pairs of shadowed areas and sunlit areas in each image were selected to calculate the optical depth, and the mean value and standard deviation of the optical depth were calculated, which were used to draw the graph of the error bar. The distribution map of optical depth values under different solar longitude was obtained (see Figure 4). According to statistical analysis, for the same shadowed area, the relative error of the retrieved optical depth is between 10% and 16% by selecting the sunlit area with obvious slope and the sunlit area with relatively flat terrain, respectively. As can be seen in Figure 4, the optical depth in the period during  $Ls \sim 150$  to  $250^{\circ}$  is larger than that in the period during  $Ls \sim 0$  to  $90^{\circ}$  in the candidate landing area of China's Mars Mission (Tianwen-1). Studies have found that dust storms in the northern hemisphere of Mars are more frequently observed during  $Ls \sim 140$  to  $270^{\circ}$  and dust storms are generally more frequent in the northern fall ( $Ls \sim 180$  to  $270^{\circ}$ ) than that in the spring ( $Ls \sim 0$  to  $90^{\circ}$ ) [1], and the number of dust storm activity recorded in the Mars Dust Activity Database have shown that most of dust activity occur in fall and winter in the northern hemisphere [28], and the seasonal variation of optical depth is similar to the seasonal variation of dust storms. The optical depth in the period of larger amount of dust activity ( $Ls \sim 150$  to  $250^{\circ}$ ) is higher than that in the period of smaller amount of dust activity ( $Ls \sim 0$  to  $90^{\circ}$ ). It is expected that the China's Mars Mission (Tianwen-1) will arrive on Mars in February 2021 and enter the orbit around Mars, and the missions of landing and inspection exploration will be carried out between May and September in 2021 ( $Ls \sim 38$  to  $93^{\circ}$ ) [29]. The optical depth during  $Ls \sim 25$  to  $93^{\circ}$  is rather small (see Figure 4), indicating that dust storm sequences are less frequently, which is conducive to the landing and inspection of the Mars probe. After Tianwen-1 enters the orbit around Mars, the optical camera onboard the orbiter will conduct the on-orbit observation of the candidate landing area. The main technical parameters of the optical cameras onboard the orbiter of Tianwen-1 are shown in Table 2 [30,31]. The images collected by High Resolution Imaging Camera (HiRIC) and Moderate Resolution Imaging Camera (MoRIC) are used to study the atmospheric optical depth of the candidate landing area after image correction (such as radiometric calibration and geometric correction), which will help assist the Mars lander and rover in carrying out missions of landing and inspection exploration to serve engineering applications.

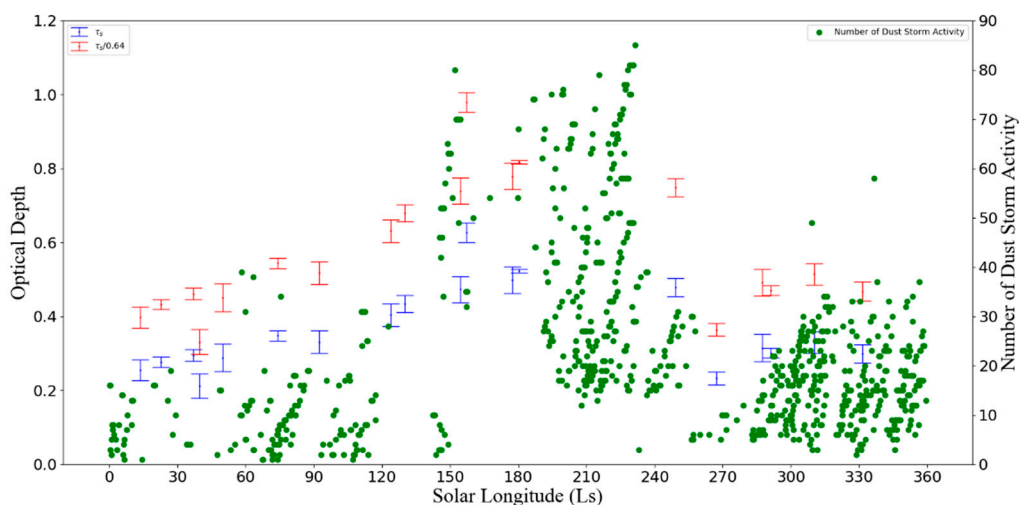


**Figure 4.** The retrieved optical depth at different solar longitude (the blue error bars represents the optical depth in the candidate landing area calculated by the shadow method, red error bars represent the optical depth divided by the correction coefficient, and green dots represents the number of dust storm activity recorded in the Mars Dust Activity Database (MDAD) at  $10^{\circ}$ – $40^{\circ}$ N [28]).

**Table 2.** The main technical parameters of the optical cameras onboard the orbiter of Tianwen-1.

Optical Cameras	The Main Technical Parameters	
HiRIC	Spectral bands	Panchromatic: 450–900 nm Color: blue 450–520 nm, green 520–600 nm, red 630–690 nm, near-infrared 760–900 nm
	Resolution (at 265 km orbit altitude)	Panchromatic: better than 2.5 m, better than 0.5 m in key areas Color: better than 10 m, better than 2.0 m in key areas
	Imaging width	9 km @ 265 km
MoRIC	Spectral range	visible spectrum (430–690 nm)
	Resolution	better than 100 m @ 400 km
	Imaging width	400 km @ 400 km orbit altitude

#### 4. Conclusions

In the same Martian year (MY29), the optical depth was calculated by the shadow method in the inspection area of the Spirit rover based on HiRISE red images and compared with the optical depth obtained by directly measuring the attenuation of sunlight by the Spirit rover. The above two measurements of optical depth have a similar pattern of seasonal variation, and the optical depth during periods of larger amount of dust activity gets significantly higher than that during periods of smaller amount of dust activity. Based on HiRISE red images, the shadow method was used to calculate the optical depth in the candidate landing area of China's Mars Mission (Tianwen-1). The results showed that the seasonal variation of optical depth was similar to that of dust storm sequences. In general, the optical depth during the period of larger amount of dust activity becomes larger than that during the period of smaller amount of dust activity. Combined with the China's Mars Mission (Tianwen-1), it can be seen that during the period of landing and inspection exploration of the Mars lander and rover ( $Ls \sim 38$  to  $93^{\circ}$ ), the optical depth is relatively small. Moreover, at a shallower optical depth, the atmosphere indicates the decline in the vertical accumulation of atmospheric dust, resulting in a lower atmospheric opacity in the planned inspection area, which is conducive to the landing and inspection

of the Mars lander and rover. The spatial resolution of HiRIC images is similar to that of HiRISE images (see Table 2). In addition, the optical depth is calculated out by HRSC images with spatial resolution of hundred meters [13], and the spatial resolution of MoRIC images is similar to that of HRSC images (see Table 2). Therefore, the images collected by HiRIC and MoRIC are used to study the atmospheric optical depth of the candidate landing area based on the technical process of retrieving optical depth in this paper, which can be applied to evaluate the atmospheric environment of Mars and assist the Mars lander and the rover of Tianwen-1 in carrying out missions of landing and inspection exploration.

**Author Contributions:** Conceptualization, J.L. and Z.T.; formal analysis, Z.T.; methodology, Z.T.; supervision, J.L., X.R., and W.Y.; writing—original draft, Z.T.; writing—review and editing, X.W. and W.C. All authors have read and agreed to the published version of the manuscript.

**Funding:** This research was funded by Beijing Municipal Science and Technology Commission (NO. Z191100004319001).

**Data Availability Statement:** The data presented in this study can be found here: [<https://github.com/cas12tang/rs> (accessed on 1 March 2021)].

**Acknowledgments:** We thank the HiRISE team for acquisition of data and the available processed data available. We are grateful to the team members of the Ground Research and Application System, who will contribute to data receiving and release of the China's Mars Mission (Tianwen-1).

**Conflicts of Interest:** The authors declare no conflict of interest.

## References

1. Wang, H.Q.; Richardson, M.I. The origin, evolution, and trajectory of large dust storms on Mars during Mars years 24–30 (1999–2011). *Icarus* **2015**, *251*, 112–127. [[CrossRef](#)]
2. Metzger, S.M.; Carr, J.R.; Johnson, J.R.; Parker, T.J.; Lemmon, M.T. Dust devil vortices seen by the Mars Pathfinder Camera. *Geophys. Res. Lett.* **1999**, *26*, 2781–2784. [[CrossRef](#)]
3. Towner, M.C. Characteristics of large Martian dust devils using Mars Odyssey Thermal Emission Imaging System visual and infrared images. *J. Geophys. Res.* **2009**, *114*. [[CrossRef](#)]
4. Landis, G.A. Dust obscuration of Mars solar arrays. *Acta Astronaut.* **1996**, *38*, 885–891. [[CrossRef](#)]
5. Navarro, T.; Forget, F.; Millour, E.; Greybush, S.J.; Kalnay, E.; Miyoshi, T. The Challenge of Atmospheric Data Assimilation on Mars. *Earth Space Sci.* **2017**, *4*, 690–722. [[CrossRef](#)]
6. Greybush, S.J.; Wilson, R.J.; Hoffman, R.N.; Hoffman, M.J.; Miyoshi, T.; Ide, K.; McConnochie, T.; Kalnay, E. Ensemble Kalman filter data assimilation of Thermal Emission Spectrometer temperature retrievals into a Mars GCM. *J. Geophys. Res.* **2012**, *117*. [[CrossRef](#)]
7. Tomasko, M.G.; Doose, L.R.; Lemmon, M.T.; Smith, P.H.; Wegryn, E. Properties of dust in the Martian atmosphere from the Imager on Mars Pathfinder. *J. Geophys. Res. Planets* **1999**, *104*, 8987–9007. [[CrossRef](#)]
8. Whelley, P.L.; Greeley, R. The distribution of dust devil activity on Mars. *J. Geophys. Res.* **2008**, *113*. [[CrossRef](#)]
9. Smith, M.D. Interannual variability in TES atmospheric observations of Mars during 1999–2003. *Icarus* **2004**, *167*, 148–165. [[CrossRef](#)]
10. Vincendon, M.; Langevin, Y.; Poulet, F.; Pommerol, A.; Wolff, M.; Bibring, J.P.; Gondet, B.; Jouglet, D. Yearly and seasonal variations of low albedo surfaces on Mars in the OMEGA/MEX dataset: Constraints on aerosols properties and dust deposits. *Icarus* **2009**, *200*, 395–405. [[CrossRef](#)]
11. Smith, M.D. THEMIS observations of Mars aerosol optical depth from 2002–2008. *Icarus* **2009**, *202*, 444–452. [[CrossRef](#)]
12. Smith, M.D. THEMIS Observations of the 2018 Mars Global Dust Storm. *J. Geophys. Res. Planets* **2019**, *124*. [[CrossRef](#)]
13. Hoekzema, N.M.; Garcia-Comas, M.; Stenzel, O.J.; Petrova, E.V.; Thomas, N.; Markiewicz, W.J.; Gwinner, K.; Keller, H.U.; Delamere, W.A. Retrieving optical depth from shadows in orbiter images of Mars. *Icarus* **2011**, *214*, 447–461. [[CrossRef](#)]
14. Montabone, L.; Forget, F.; Millour, E.; Wilson, R.J.; Lewis, S.R.; Cantor, B.; Kass, D.; Kleinbohl, A.; Lemmon, M.T.; Smith, M.D.; et al. Eight-year climatology of dust optical depth on Mars. *Icarus* **2015**, *251*, 65–95. [[CrossRef](#)]
15. Lemmon, M.T.; Wolff, M.J.; Smith, M.D.; Clancy, R.T.; Banfield, D.; Landis, G.A.; Ghosh, A.; Smith, P.H.; Spanovich, N.; Whitney, B.; et al. Atmospheric imaging results from the Mars exploration rovers: Spirit and Opportunity. *Science* **2004**, *306*, 1753–1756. [[CrossRef](#)]
16. Lemmon, M.T.; Wolff, M.J.; Bell, J.F.; Smith, M.D.; Cantor, B.A.; Smith, P.H. Dust aerosol, clouds, and the atmospheric optical depth record over 5 Mars years of the Mars Exploration Rover mission. *Icarus* **2015**, *251*, 96–111. [[CrossRef](#)]
17. Pollack, J.B.; Colburn, D.; Kahn, R.; Hunter, J.; Van Camp, W.; Carlston, C.E.; Wolf, M.R. Properties of aerosols in the Martian atmosphere, as inferred from Viking Lander imaging data. *J. Geophys. Res.* **1977**, *82*, 4479–4496. [[CrossRef](#)]

18. Smith, P.H.; Lemmon, M. Opacity of the Martian atmosphere measured by the Imager for Mars Pathfinder. *J. Geophys. Res. Planets* **1999**, *104*, 8975–8985. [[CrossRef](#)]
19. McEwen, A.S.; Eliason, E.M.; Bergstrom, J.W.; Bridges, N.T.; Hansen, C.J.; Delamere, W.A.; Grant, J.A.; Gulick, V.C.; Herkenhoff, K.E.; Keszthelyi, L.; et al. Mars Reconnaissance Orbiter’s High Resolution Imaging Science Experiment (HiRISE). *J. Geophys. Res.* **2007**, *112*. [[CrossRef](#)]
20. Snyder, J.P. Map projections—A working manual. In *U.S. Geological Survey Professional Paper 1395*; U.S. Government Printing Office: Washington, DC, USA, 1987. [[CrossRef](#)]
21. Arvidson, R.E.; Anderson, R.C.; Bartlett, P.; Bell, J.F.; Blaney, D.; Christensen, P.R.; Chu, P.; Crumpler, L.; Davis, K.; Ehlmann, B.L.; et al. Localization and physical properties experiments conducted by Spirit at Gusev crater. *Science* **2004**, *305*, 821–824. [[CrossRef](#)]
22. Bell, J.F.; Squyres, S.W.; Herkenhoff, K.E.; Maki, J.N.; Arneson, H.M.; Brown, D.; Collins, S.A.; Dingizian, A.; Elliot, S.T.; Hagerott, E.C.; et al. Mars Exploration Rover Athena Panoramic Camera (Pancam) investigation. *J. Geophys. Res. Planets* **2003**, *108*. [[CrossRef](#)]
23. Clancy, R.T.; Sandor, B.J.; Wolff, M.J.; Christensen, P.R.; Smith, M.D.; Pearl, J.C.; Conrath, B.J.; Wilson, R.J. An intercomparison of ground-based millimeter, MGS TES, and Viking atmospheric temperature measurements: Seasonal and interannual variability of temperatures and dust loading in the global Mars atmosphere. *J. Geophys. Res. Planets* **2000**, *105*, 9553–9571. [[CrossRef](#)]
24. Ye, P.J.; Sun, Z.Z.; Rao, W.; Meng, L.Z. Mission overview and key technologies of the first Mars probe of China. *Sci. China Technol. Sci.* **2017**, *60*, 649–657. [[CrossRef](#)]
25. McEwen, A.S.; Soderblom, L.A.; Becker, T.L.; Lee, E.M.; Swann, J.D.; Aeschliman, R.; Batson, R.M. Global Color Views of Mars. In *Proceedings of the 25th Lunar and Planetary Science Conference*, Houston, TX, USA, 14–18 March 1994; p. 871.
26. McCleese, D.J.; Heavens, N.G.; Schofield, J.T.; Abdou, W.A.; Bandfield, J.L.; Calcutt, S.B.; Irwin, P.G.; Kass, D.M.; Kleinbohl, A.; Lewis, S.R.; et al. Structure and dynamics of the Martian lower and middle atmosphere as observed by the Mars Climate Sounder: Seasonal variations in zonal mean temperature, dust, and water ice aerosols. *J. Geophys. Res. Atmos.* **2010**, *115*. [[CrossRef](#)]
27. Smith, M.D.; Wolff, M.J.; Clancy, R.T.; Kleinbohl, A.; Murchie, S.L. Vertical distribution of dust and water ice aerosols from CRISM limb-geometry observations. *J. Geophys. Res. Planets* **2013**, *118*, 321–334. [[CrossRef](#)]
28. Battalio, M.; Wang, H.Q. The Mars Dust Activity Database (MDAD): A comprehensive statistical study of dust storm sequences. *Icarus* **2021**, *354*, 114059. [[CrossRef](#)]
29. Wan, W.X.; Wang, C.; Li, C.L.; Wei, Y. China’s first mission to Mars. *Nat. Astron.* **2020**, *4*, 721. [[CrossRef](#)]
30. Li, C.L.; Liu, J.J.; Geng, Y.; Cao, J.B.; Zhang, T.L.; Fang, G.Y.; Yang, J.F.; Shu, R.; Zou, Y.L.; Lin, Y.T.; et al. Scientific Objectives and Payload Configuration of China’s First Mars Exploration Mission. *J. Deep Space Explor.* **2018**, *5*, 406–413. (In Chinese) [[CrossRef](#)]
31. Zou, Y.L.; Zhu, Y.; Bai, Y.F.; Wang, L.G.; Jia, Y.Z.; Shen, W.H.; Fan, Y.; Liu, Y.; Wang, C.; Zhang, A.B.; et al. Scientific objectives and payloads of Tianwen-1, China’s first Mars exploration mission. *Adv. Space Res.* **2021**, *67*, 812–823. [[CrossRef](#)]